

SANA-Streaming: Real-time Streaming Video Editing with Hybrid Diffusion Transformer

Yuyang Zhao^{1*}, Yicheng Pan^{3*}, Qiyuan He^{1,4*}, Jincheng Yu^{1*}, Junsong Chen^{1,5*},
Tian Ye¹, Haozhe Liu¹, Enze Xie¹, Song Han^{1,2}

¹NVIDIA ²MIT ³THU ⁴NUS ⁵HKU

*Equal contribution

Project Page: <https://nvlabs.github.io/Sana/Streaming>

Real-time streaming video-to-video editing (V2V) is critical for interactive applications such as live broadcasting and gaming, yet it remains a formidable challenge due to the stringent requirements for temporal consistency and inference throughput. In this paper, we present **SANA-Streaming**, a system-algorithm co-designed framework for high-resolution, real-time streaming video editing on consumer GPUs, with the following three core designs: (1) **Hybrid Diffusion Transformer architecture** introduces softmax attention in part of the blocks to improve local modeling capabilities while preserving the efficiency of linear layers. (2) **Cycle-Reverse Regularization** is a novel training strategy that enforces semantic consistency by predicting source frames from generated content via flow matching, improving temporal consistency without requiring paired long edited videos. (3) **Efficient System Co-design** combines fused GDN kernels and Mixed-Precision Quantization (MPQ) optimized for the NVIDIA Blackwell (RTX 5090) architecture. By profiling real-world throughput, our MPQ maximizes Tensor Core utilization while maintaining generation quality. The resulting system achieves real-time 1280×704 resolution editing at **24 end-to-end FPS** on a single RTX 5090 GPU, with the DiT core running at **58 FPS**. Experimental results demonstrate that our co-design approach significantly outperforms existing SOTA methods in both temporal coherence and system throughput.

arXiv:2605.30409v1 [cs.CV] 28 May 2026

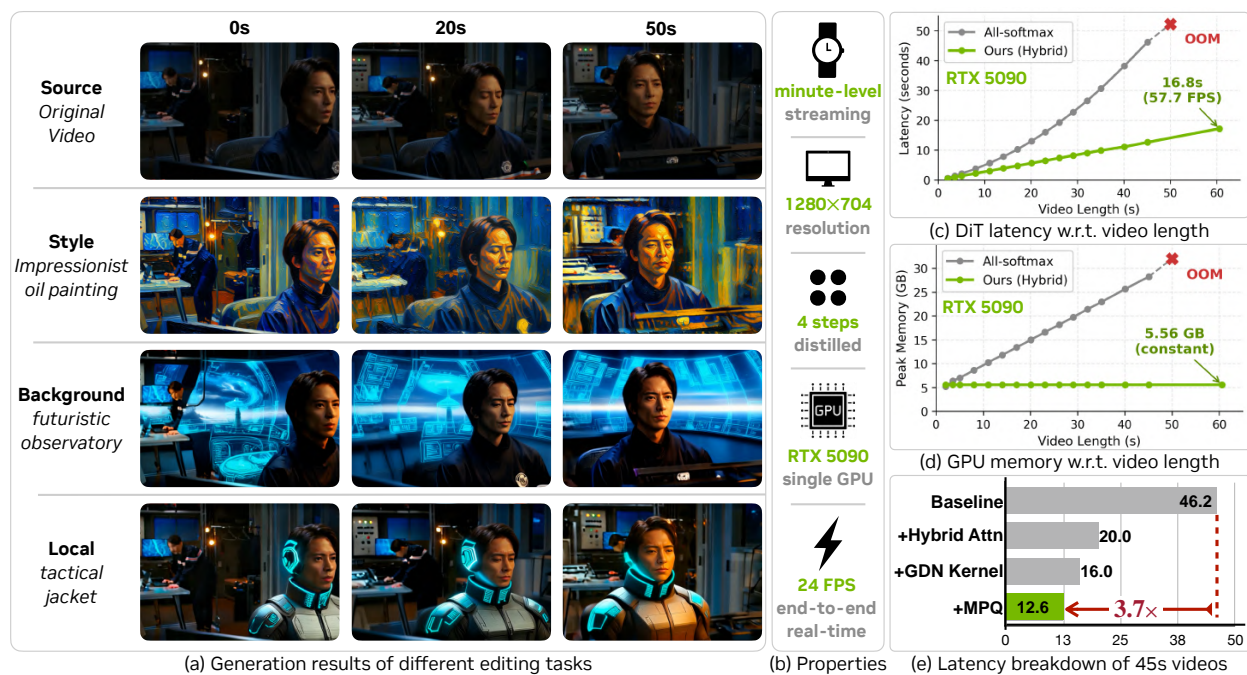


Figure 1 | **Overview of SANA-Streaming.** Our method supports temporally consistent minute-length video editing at 1280×704 resolution while maintaining bounded memory and real-time throughput on a single RTX 5090.

1. Introduction

Instruction-guided video editing aims to transform an input video according to a natural-language instruction while preserving the motion and content that should remain unchanged. Recent video editing systems have made rapid progress on short clips, driven by stronger video diffusion transformers and large-scale synthetic editing data [17, 29, 2, 14, 19, 25]. However, real-time streaming V2V editing remains substantially harder. The model must generate frames in chronological order, maintain long-range appearance consistency across hundreds of frames, and fit within the latency and memory budget of a consumer GPU. These requirements rule out many accurate but bidirectional or full-attention designs that work well for short clips. To this end, we present SANA-Streaming, a system-algorithm co-designed framework for real-time, high-resolution streaming video editing.

A natural starting point is SANA-Video [6], the efficient video generation backbone on which our system is built. SANA-Video replaces vanilla attention with linear attention and introduces block linear attention with a constant-memory state cache, making long high-resolution video generation practical on edge GPUs. Its long-video extension, LongSANA, further adapts this all-linear backbone to streaming generation through causal chunking, recurrent state reuse, and LongLive-style [34] streaming long tuning. This design is attractive for throughput, but it exposes a key limitation for V2V editing: linear attention compresses history into finite recurrent states and is less localized than softmax attention, making it harder to preserve fine-grained source correspondence across chunk boundaries. In practice, this manifests as visible chunk-to-chunk appearance jumps and temporal flicker in long causal generation (Figure 12). Conversely, replacing all blocks with softmax attention improves local modeling but becomes memory-prohibitive for long high-resolution streams (Figure 1(d)). This tension motivates a hybrid design that allocates expressive softmax attention only where it is most useful, while preserving recurrent linear-state caching in the majority of layers.

Hybrid Diffusion Transformer. The DiT model of SANA-Streaming is a hybrid diffusion transformer derived from the SANA-Video’s all-linear backbone, where we insert softmax-attention blocks evenly in the all linear backbones and replace the vanilla linear attention with an efficient variant of Gated DeltaNet (GDN) [35]. In this hybrid design, SANA-Streaming leverage GDN blocks to maintain the important global information with dynamic gate and decay. Softmax attention blocks are adopted to efficiently explore the locality and first block consistency with window attention and attention sink. Such design keeps memory constant and generation speed for arbitrary generation length while still keeping long range consistency. As shown in Figure 1, compared with all softmax attention variant, the hybrid design only requires 5.56 GB VRAM for long video generation and 3.7 times faster generation speed, enabling real-time execution on the consumer GPUs.

Cycle Consistent Streaming Training. Due to the lack of paired long video editing data, we adopt LongLive [34] as our basic streaming training framework, which uses short video generation teacher to supervise the rollout long video clips with Distribution Matching Distillation (DMD) [39, 38] loss. However, the short teacher supervision lacks the long-range information and therefore may lead drifting when supervise long rollout clips. In view of this limitation, we introduce Cycle-Reverse Regularization. Starting from the LongLive training strategy, our method adds a reverse editing objective: after generating an edited chunk, the model is required to reconstruct the corresponding source chunk conditioned on a reverse prompt. Since the long video itself is a real-world temporal consistent video, the reverse loss can force the model to learn how to maintain the long range temporal consistency. In addition to the DiT training, we also distill our VAE decoder from bidirectional convolution to causal convolution, supporting streaming decoding.

Efficient System Co-design. To enhance the generation efficiency on the consumer GPUs, we explore the inference system design. On the one hand, we improve the efficiency of frame-wise GDN kernel with partition strategy, so that the state matrices can be stored on the GPU’s SRAM, leading to **1.5-2.2x** speed up on different GPU architectures. In addition, since the NVFP4 and FP8 Tensor Core is super efficient on Blackwell architecture while the BF16 precision has the best quality, we design a precision search algorithm inspired from AutoML. By evaluating the trade-off between generation quality and efficiency, we find the best mixed precision strategy for different layers and different blocks, leading to **59%** speed up over BF16 on the DiT model with marginal quantization error.

Data Pipeline. The success of SANA-Streaming relies on the strong data pipeline for both short videos and long videos. For short videos, we leverage the image editing model to edit the first frame and I2V generation

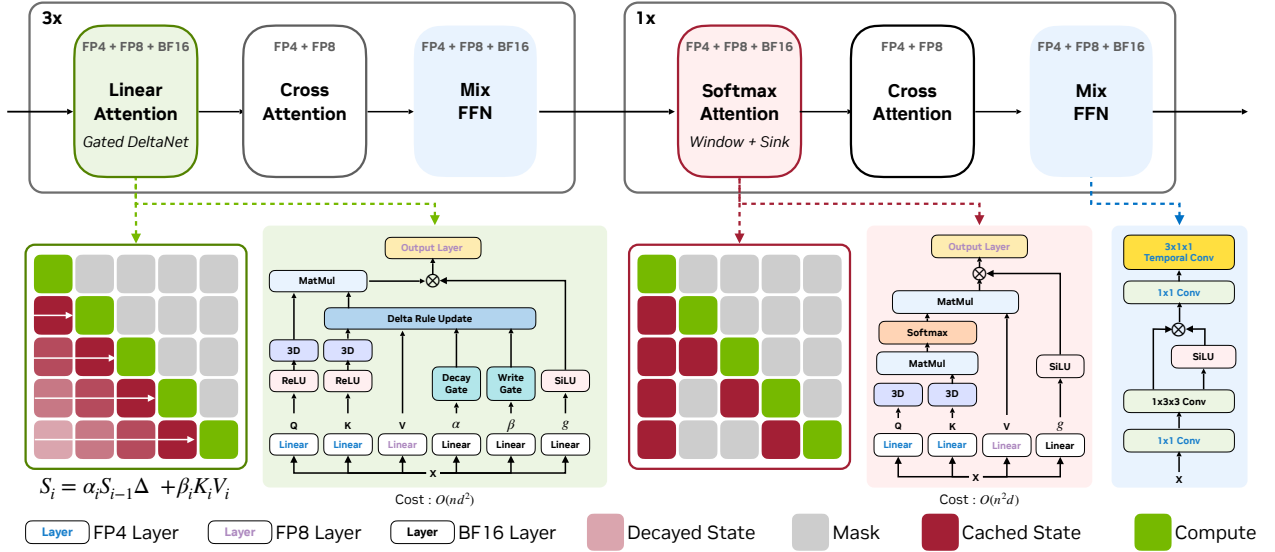


Figure 2 | **Hybrid streaming diffusion transformer.** SANA-Streaming interleaves GDN blocks and softmax attention blocks. The two types of blocks focus on different aspect of information with a fixed computational cost. For the detailed block design, each layer will use the most suitable precision for efficiency and generation quality.

model to obtain the pairs, as well as data verification to filter out low quality pairs. For the long video, since generating consistent pairs is difficult, we use VLM to generate forward and reverse editing prompts for streaming long training and our cycle-reverse regularization.

Our contributions are summarized as follows.

- We propose a hybrid diffusion transformer for streaming video editing, combining global information from GDN blocks with strong locality information from softmax-attention blocks for efficient and high quality generation.
- We introduce Cycle-Reverse Regularization, which leverages long source videos through a reverse flow-matching objective and improves long-range consistency without requiring paired long edited videos.
- We propose a comprehensive editing data generation pipeline for both short video pairs and long video prompts, which is the basic of streaming video editing.
- We develop an efficient system design with fused GDN kernels and Mixed-Precision Quantization, achieving 24 end-to-end FPS and 58 DiT FPS on an RTX 5090 GPU.

2. Methodology

2.1. Hybrid Architecture

This section introduces the key architectural design of SANA-Streaming for minute-length streaming video editing. Motivated by the complementary limitations of softmax attention and linear attention, we develop a hybrid diffusion transformer enabling long video editing with global consistency and local granularity under fixed GPU memory.

Limitations of Softmax Attention and Linear Attention. Causal softmax attention provides strong token-level interaction and precise source correspondence, which is crucial for high-quality video-to-video editing. However, attending to all historical high-resolution video tokens is memory-prohibitive, as the active KV cache grows with video length. In addition, as shown in Figure 3(a), softmax attention commonly focuses more on local information. Therefore, restricting softmax attention to a local window with a persistent sink token is applicable while significantly reducing memory cost in long video generation. However, global information is excluded in such attention operation. In contrast, linear attention is naturally suitable for streaming because it compresses the generated prefix into a compact recurrent state whose size is independent of the number of chunks. Nevertheless, the dense attention maps (Figure 3(b)) demonstrate that linear attention does not focus enough on the neighborhood, leading to chunk-boundary flickering (Figure 12).

We therefore combine the two mechanisms in an interleaved hybrid design as Figure 2 shows, following Qwen-Next [33]. In SANA-Streaming, most blocks use Gated DeltaNet (GDN) linear attention to maintain compact global memory for consistency, while a small number of blocks use sliding window softmax attention with a persistent sink chunk and a short recent window. This preserves the efficiency of an all-linear streaming DiT while enabling fine-grained attention to local context.

Frame-wise Gated DeltaNet for Global Accumulated Memory.

The linear-attention blocks in SANA-Streaming serve as the global memory pathway for causal streaming. Instead of token-wise updates or caching raw tokens from all previous chunks, each block maintains a compact recurrent state that is updated frame-by-frame and carried across chunks. This state summarizes the generated prefix into a fixed-size memory, enabling long-range information propagation under fixed GPU memory.

Given the latent $x \in \mathbb{R}^{F \times N \times C}$ in each head, we obtain the query $q \in \mathbb{R}^{F \times N \times C}$, key $k \in \mathbb{R}^{F \times N \times C}$, value $v \in \mathbb{R}^{F \times N \times C}$, decay gate $\alpha \in \mathbb{R}^F$, write gate $\beta \in \mathbb{R}^{F \times N}$ and output gate $g \in \mathbb{R}^{F \times N \times C}$, where F , N , and C denote the number of frames, number of tokens in each frame and head dimension respectively. The numerator state of the f th frame S_f^{kv} and denominator normalizer state S_f^z can be updated with the delta-rule correction [35]:

$$S_f^{kv} = \alpha_f S_{f-1}^{kv} (I - \beta_f \hat{k}_f \hat{k}_f^\top) + \beta_f v_f \hat{k}_f^\top, \quad S_f^z = \alpha_f S_{f-1}^z (I - \beta_f k_f k_f^\top) + \beta_f k_f^\top. \quad (1)$$

where k_f and \hat{k}_f is the key before and after RoPE [22]. This update differs from simple accumulation: rather than directly writing $v_f k_f^\top$ into memory, the model only writes the residual. As a result, the recurrent state behaves as a correction-based memory, which is more robust for long streaming sequences. More details are available in Appendix G. The final output is then read from the updated state through a normalized readout followed by an output gate and a linear projection:

$$o_f = W_o \left(g_f \odot \frac{S_f^{kv} \hat{q}_f}{(S_f^z)^\top q_f + \epsilon} \right), \quad (2)$$

where q_f and \hat{q}_f is the query before and after RoPE [22]. During streaming inference, each Gated DeltaNet block only caches the terminal recurrent states (S^{kv}, S^z) of the previous chunk and uses them to initialize the next chunk. Therefore, the memory cost of the linear-attention pathway remains independent of the number of streamed chunks. In our hybrid architecture, these Gated DeltaNet blocks provide a compact global accumulated memory.

Softmax blocks for local window and sink refinement. GDN blocks provide efficient global memory and softmax attention blocks help for more locality information. Instead of using all the frames for attention, each chunk attends to a constrained context consisting of itself, a persistent sink, and a local window. The sink chunk provides a stable visual anchor shared across the stream, while the recent window preserves high-resolution local evidence from neighboring chunks. This design restores precise local matching with fixed GPU memory.

2.2. Long-term Consistency Training

Streaming long training. We train SANA-Streaming under the same causal streaming protocol used during inference. Given a long source video and an editing prompt, the model generates edited latent chunks autoregressively. Upon generating each chunk, the streaming cache is updated with the generated chunk, and a LongLive-style distribution matching distillation (DMD) self-forcing loss [34, 15] is applied to the current chunk. mitigates the discrepancy between short-clip training and minute-length streaming inference, enabling the model to learn from its own generated history.

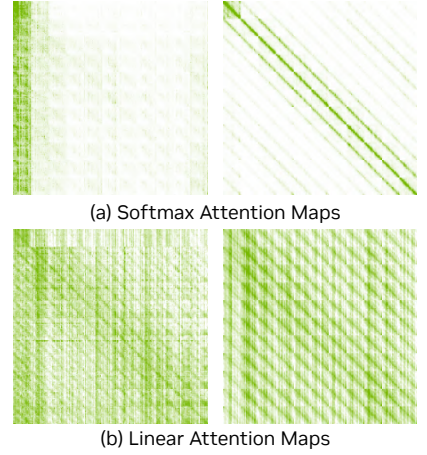


Figure 3 | Attention map visualization of different heads.

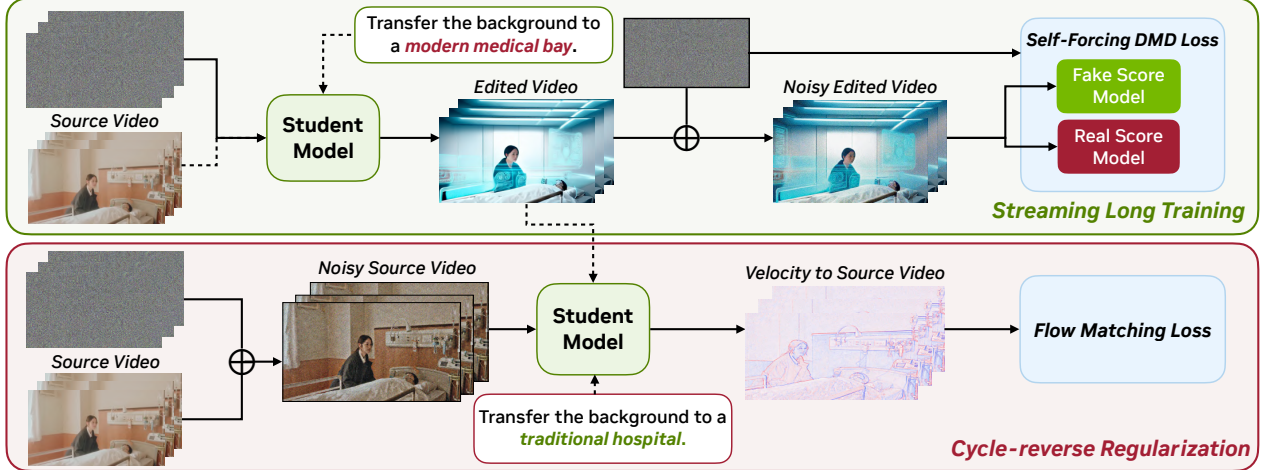


Figure 4 | **Streaming Long Training and Cycle-Reverse Regularization.** The forward streaming branch uses streaming long training with DMD loss. The reverse branch reuses the generated edited chunk as visual condition and applies a reverse instruction to reconstruct the original source chunk with a flow-matching loss, which improves temporal consistency without paired long edited targets.

Cycle-reverse regularization. While streaming long training improves long-horizon generation, video-to-video editing further requires the edited stream to preserve the source structure and motion over time. Although minute-length source videos are relatively easy to collect, paired target videos that faithfully follow the editing instruction are rarely available. We therefore introduce a cycle-reverse regularization strategy that uses only long source videos without paired edited videos.

Specifically, the model first performs a forward streaming edit from the source video to the target domain according to the editing prompt. Then, the generated edited chunk is used as the visual condition for a reverse edit, guided by a reverse prompt that describes how to recover the original source domain, as shown in Figure 4. The reverse pass is trained with a flow-matching objective toward the original source chunk. Overall, streaming long training teaches the model to follow editing instructions under causal rollout and cycle-reverse regularization encourages the edited video to preserve long-term structure and motion consistency learned from real-world source videos.

Causal VAE Distillation. The video VAE decoder is another bottleneck for streaming video editing. The original LTX2 VAE decoder uses bidirectional temporal context, while streaming inference cannot access future latent frames. We convert it into a causal decoder by replacing symmetric temporal padding with left-only padding, so each output frame only depends on current and previous latent frames. For stable initialization, we reuse the pretrained LTX2 VAE weights and remap each temporal 3-tap convolution from bidirectional weights $[a, b, c]$ to causal weights $[0, a, b+c]$, preserving the previous-frame and current-frame roles while folding the unavailable future-frame contribution into the current frame, as shown in Figure 5. We then distill the causal decoder from the original bidirectional decoder. The training objective combines Charbonnier reconstruction loss [3], perceptual loss [18], Haar wavelet high-frequency loss [37, 41], and intermediate decoder feature distillation [45]:

$$\mathcal{L}_{\text{vae}} = \lambda_{\text{charb}} \mathcal{L}_{\text{charb}} + \lambda_{\text{perc}} \mathcal{L}_{\text{perc}} + \lambda_{\text{haar}} \mathcal{L}_{\text{haar}} + \lambda_{\text{distill}} \mathcal{L}_{\text{distill}}. \quad (3)$$

2.3. Efficient System Co-design

Efficient GDN Kernel. The recurrent GDN update is algorithmically efficient, but a literal implementation is not hardware efficient. For both H100 and RTX 5090, the recurrent state (S_f, z_f) is small enough to keep in on-chip storage, while the per-frame Q_f, K_f, V_f activations span hundreds of spatial tokens and must be streamed from HBM. Following the IO-aware principle of FlashAttention [10, 9], we tile the spatial dimension so that each block of activations is loaded once, reduced into compact frame-level summaries, and then

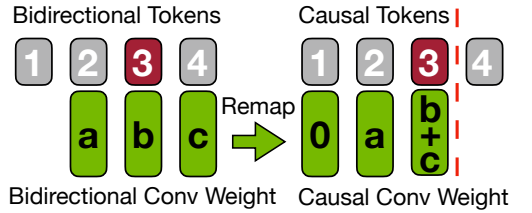


Figure 5 | Remapping weights in VAE.

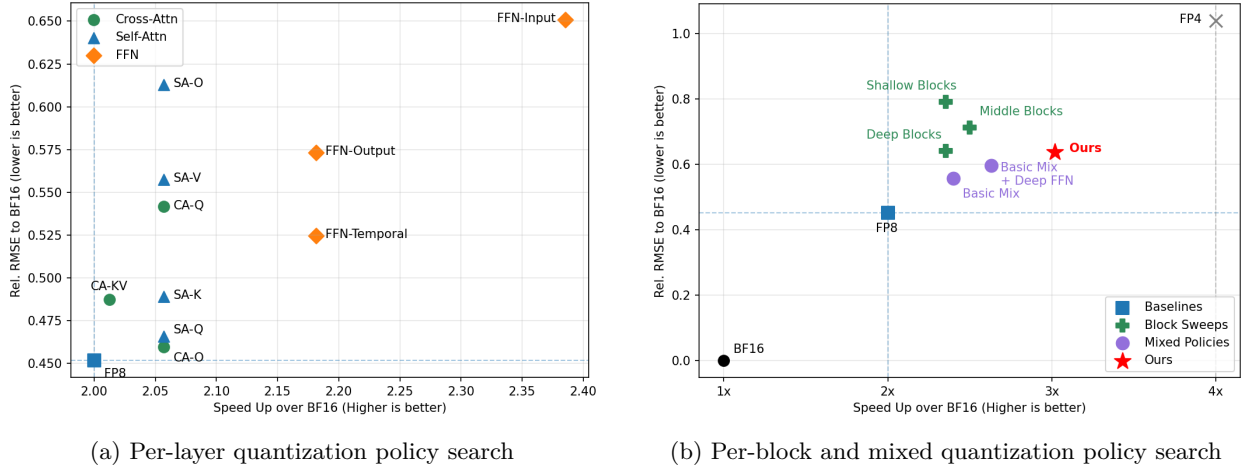


Figure 6 | **Mixed-Precision Quantization Policy Search on Relative RMSE.** For each subfigure, the x-axis is the estimated speed up and the y-axis is the quantization error over the BF16 reference. The selected mixed-precision policy achieves the best trade-off between efficiency and quality.

discarded.

We rewrite the update by separating the spatial reduction from the temporal recurrence:

$$P_f = I - K_f^\top \text{diag}(\beta_f) K_f, \quad A_f = K_f^\top \text{diag}(\beta_f) V_f, \quad (4)$$

$$S_f = \alpha_f P_f S_{f-1} + A_f. \quad (5)$$

The vector path computes $P_f^z = I - K_f^\top \text{diag}(\beta_f) K_f$ and $b_f = K_f^\top \beta_f$, then $z_f = \alpha_f P_f^z z_{f-1} + b_f$. This decomposition exposes most of the work as frame-parallel: P_f, A_f, P_f^z, b_f are computed independently per frame and head, while only the compact scan over (S_f, z_f) remains sequential.

Our Triton implementation uses a three-phase chunkwise pipeline. Phase A computes the frame summaries with blocked reductions over the spatial dimension. Phase B performs the short recurrent scan over frames while keeping the state in on-chip storage. Phase C streams Q_f blocks and applies the compact states to produce the output. For bidirectional GDN, we exploit the linearity of Phase C and combine the forward and reverse histories before the output pass, avoiding a second output kernel and a second read of Q_f . This chunkwise design consistently gives large layer-level speedups and roughly $1.5\times-2.2\times$ end-to-end sampling speedups over the PyTorch reference.

Mixed-Precision Quantization Policy Search. Quantization is further explored in this paper to support the efficiency on consumer GPUs. NVFP4 quantization is fast on Blackwell architecture but not uniformly reliable, for two main reasons: (1) some layers are more sensitive and should remain in higher precision, such as the patch embedding layer and output layer; (2) some layers has very few parameters with small computational cost, so the quantization overhead exceeds the kernel speedup, such as gate layer. We therefore search at layer-type and block-position granularity instead of assigning the same precision to the whole DiT. We first set the most sensitive or unsupported layers to BF16, including the patch embedding layer, output layer, timestep embedding layer, the gates in attention blocks and depth-wise convolution in MixFFN. For the remaining layers, we start from an FP8 base and apply group wise NVFP4 on it. The searchable FP4 groups include per-layer groups: self-attention $Q/K/V/O$, cross-attention $Q/KV/O$, FFN input and output projections, and temporal FFN projections; block-wise groups: shallow (0-5), middle (6-13) and deep blocks (14-19). For each candidate π , we run a 30-second streaming video generation with the same noise on a calibration set. Let \hat{x}_0^{ref} be the BF16 output latent and \hat{x}_0^π be the output latent under policy π . We score the candidate by latent relative RMSE and LPIPS [18]:

$$\text{RelRMSE}(\pi) = \frac{\sqrt{\frac{1}{N} \|\hat{x}_0^\pi - \hat{x}_0^{\text{ref}}\|_2^2}}{\text{Std}(\hat{x}_0^{\text{ref}}) + \epsilon}. \quad (6)$$

Figure 6 and Figure 11 illustrate how each group influences efficiency and quality. We make the following observations. **First**, the key and query of self-attention (SA-K, SA-Q) and the output projection of cross-

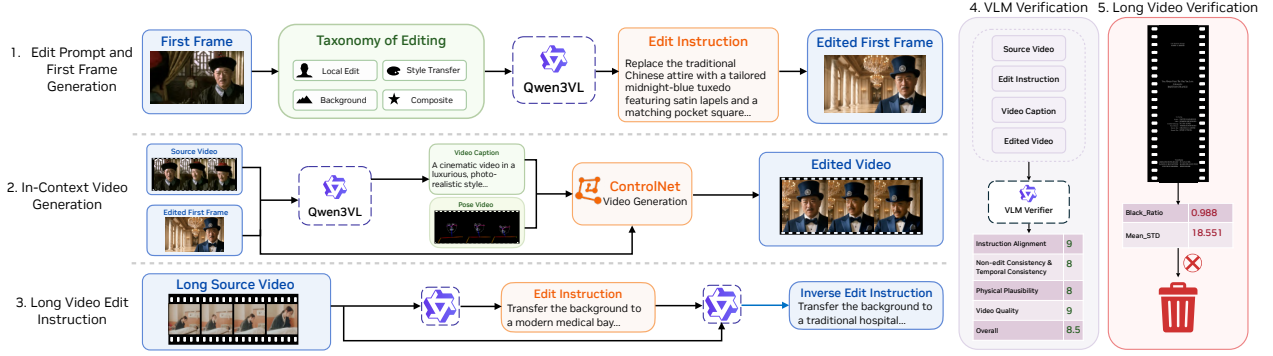


Figure 7 | **Data Pipeline.** For short videos, we sample taxonomy-guided edit instructions, edit the first frame as a visual anchor, and generate edited videos by conditioning on the source video, edited first frame, caption, and pose video. For long videos, we generate paired forward and inverse instructions from source videos to support streaming long training and cycle-reverse regularization. Both short and long samples are filtered by VLM-based verification, and long videos are additionally screened for invalid black-frame segments.

attention (CA-O) sit nearly on top of the FP8 baseline while still delivering a $\sim 2.06\times$ speedup, so they are the safest layers to demote and form our *Basic Mix*, joined by FFN-Temporal – the only FFN component whose quantization error is negligible relative to its efficiency gain. **Second**, the remaining attention projections (SA-V, SA-O, CA-Q) move noticeably above the FP8 horizontal, indicating that the value and post-mixing pathway is sensitive to FP4 noise; we keep them in FP8. **Third**, CA-KV sits closest to FP8 on both axes but covers only 1% of the DiT FLOPs, so demoting it brings little speedup and we exclude it from the policy. **Fourth**, the FFN input/output point-wise convolutions are the heaviest modules in the network ($\sim 49\%$ of FLOPs combined); demoting them globally collapses quality. **However**, the block-range sweep reveals a clear depth ordering: shallow blocks are the most fragile, while deep and middle blocks tolerate FP4 well, opening a depth-restricted demotion path. To this end, the resulting policy (red star in Figure 6) uses FP4 for the most robust groups, including cross-attention output, self-attention query and key, temporal FFN projection in all blocks as well as FFN input and output projections in middle and deep blocks. The unsupported and most sensitive layers listed at the start of this section (patch embedding, output projection, timestep embedding, attention gates, MixFFN depth-wise convolution) remain in BF16, and all other linear layers not assigned to FP4 stay in FP8. The mixed-precision policy gains 3x efficiency on the quantized layers and 1.59x efficiency on DiT latency over BF16 baseline. The detailed analysis of each layer and block are available in Appendix A.

3. Data Pipeline

Since one of the main downstream tasks of SANA-Streaming is live broadcasting, we introduce our data pipeline to further generate high-quality human-centric video editing pairs as well as the editing prompts for long videos. Figure 7 summarizes the complete pipeline, including short-video pair construction, long-video instruction construction, and VLM-based filtering. The details of our data generation pipeline are available at Appendix E.

4. Experiments

4.1. Implementation Details

SANA-Streaming is a 2B hybrid diffusion transformer with LTX2 VAE [13] (compression ratio $32\times 32\times 8$). The DiT contains 20 transformer blocks with evenly inserted 5 softmax attention blocks and 15 GDN blocks. The condition video latent is concatenated to the latent on the channel dimension. The model is trained by two stages on 1280×704 resolution: bidirectional short training and streaming long training. In the bidirectional short training stage, we use bidirectional GDN with forward and backward scan. In the streaming long training stage, 3 latent frames are regarded as a chunk. The forward scan with previous cache and backward scan within the chunk is adopted by GDN. The streaming model is distilled to 4 steps. With the algorithm and system co-design, SANA-Streaming achieves 24 end-to-end FPS and 58 DiT FPS on an RTX 5090 GPU. For

Table 1 | OpenVE-Bench comparison on the five spatially aligned edit categories used in our evaluation. The color and color highlights indicate the best and second-best quality scores, respectively. Latency is measured with batch size 1, while throughput is measured with batch inference on eight H100 GPUs for 81-frame 1280×704 videos. † indicates the step distilled model.

Methods	#Params.	#Reso.	Latency (s)	Throughput (FPS)	Avg.	Global Style	BG Change	Local Change	Local Remove	Local Add
VACE [17]	14B	1280x720	1991	0.3	1.57	1.49	1.55	2.07	1.46	1.26
OmniVideo [24]	1.3B	640x352	—	—	1.19	1.11	1.18	1.14	1.14	1.36
InsViE [29]	2B	720x480	750	0.9	1.45	2.20	1.06	1.48	1.36	1.17
Lucy-Edit [25]	5B	1280x704	97	6.7	2.22	2.27	1.57	3.20	1.75	2.30
ICVE [19]	13B	384x240	6051	0.2	2.18	2.22	1.62	2.57	2.51	1.97
DITTO [2]	14B	832x480	1971	0.3	2.13	4.01	1.68	2.03	1.53	1.41
OpenVE-Edit [14]	5B	1280x704	97	6.7	2.50	3.16	2.36	2.98	1.85	2.15
SANA-Streaming	2B	1280x704	20	32.4	2.62	3.48	2.29	3.20	2.27	1.88
SANA-Streaming †	2B	1280x704	1	762.8	2.42	3.60	1.82	3.10	1.78	1.82

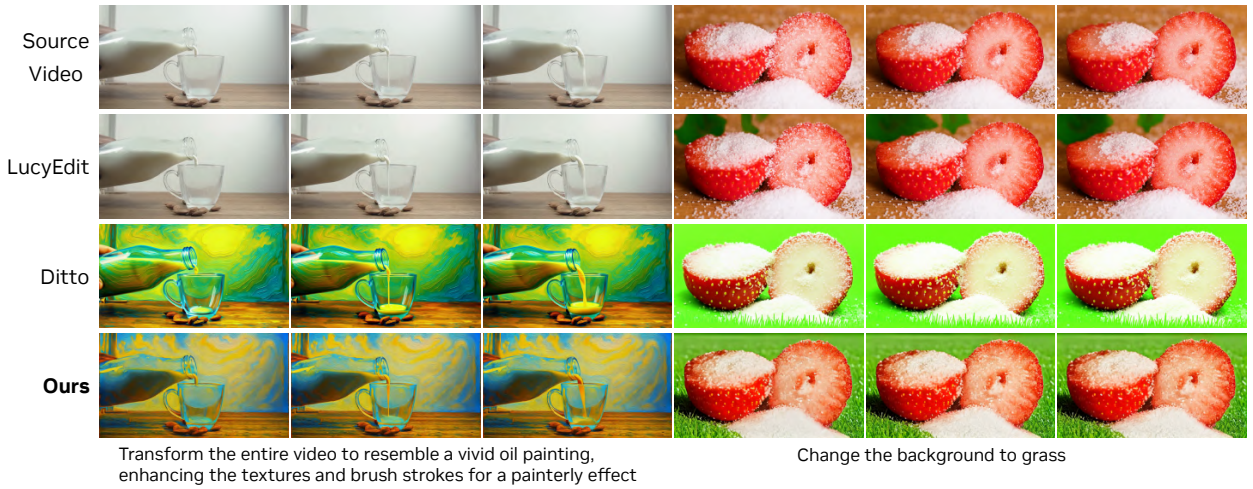


Figure 8 | **Qualitative comparison with prior video editors.** SANA-Streaming preserves source motion and non-edited content while following the edit instructions.

quantitative evaluation, we use the five OpenVE-Bench [14] pixel-aligned categories: global style, background change, local change, local remove, and local add.

4.2. Performance Comparison and Analysis

Table 1 compares SANA-Streaming with representative instruction-guided video editing systems on the five OpenVE-Bench categories used in our evaluation. SANA-Streaming first stage model is a bidirectional model on short videos, and it achieves the state-of-the-art performance on this benchmark, with nearly 2.5x smaller model size and 5x faster throughput than the previous best method (OpenVE [14]). The streaming and distilled version of our model targets deployment on consumer GPUs. However, even with distillation, SANA-Streaming can still achieve comparable performance with previous methods and has more than 100x higher throughput. Qualitative comparisons are shown in Figure 8 and more qualitative long video results of SANA-Streaming are available in Figure 13.

4.3. Ablation Studies

Efficient System Co-design. Efficient system co-design is crucial to achieve real-time end-to-end generation on consumer GPUs. In Table 2, we break down the deployment optimizations over the BF16 baseline. Specifically, the lossless efficient GDN kernel improves the DiT latency by 22%, and Mixed-Precision Quantization (MPQ) further reduces the DiT latency to 16.8s, yielding a 1.59× DiT speedup over the BF16 baseline and achieving 24 FPS for end-to-end generation. These results demonstrate the importance and effectiveness of

Table 2 | Latency (s) analysis of the efficient system co-design on an RTX 5090 for 1-minute video.

System Setting	VAE Encode	VAE Decode	DiT Latency	End-to-end Latency	DiT Speedup
BF16			26.8	50.7	1.00×
+ GDN Kernel	15.4	8.5	21.9	45.8	1.22×
+ MPQ			16.8	40.7	1.59×

Table 3 | Causal VAE Distillation Comparison.

Methods	PSNR	LPIPS	SSIM
Bidirectional	32.98	0.0274	0.923
Causal (Before Training)	24.66	0.132	0.785
Causal (After Training)	32.14	0.0336	0.911

Figure 9 | **Effect of Cycle-Reverse Regularization.** Adding cycle-reverse regularization improves the preservation of source motion and non-edited regions while keeping the video temporally stable.

our algorithm-system co-design.

Cycle-Reverse Regularization. Cycle-Reverse Regularization aims to improve temporal consistency when the paired long videos are not available. As shown in the first case of Figure 9, cycle-reverse regularization can keep the non-edited region consistent with the source video. In the second case, the edited “crystal tree” changes in the later frames when regularization is not applied but our model keeps it consistent throughout the whole long video.

Causal VAE. We compare the fine-tuned causal VAE decoder against the original decoder with causal and non-causal decoding in Figure 10. Direct causal conversion introduces visible blur and loss of fine detail because the decoder no longer has access to future latent frames. After causal decoder distillation, the streaming VAE recovers sharper textures and object boundaries, achieving comparable performance with the bidirectional teacher (Figure 10 and Table 3).

5. Related Work

Hybrid Linear-Softmax Architectures. Diffusion Transformers (DiTs) have become the dominant paradigm for high-quality image [31, 32, 5, 37, 28] and video generation [27, 12, 13]. However, full attention incurs quadratic complexity, leading to prohibitive memory and latency costs for long sequences. To improve efficiency, prior work such as SANA-Video [6, 43] replaces full attention with linear attention and SLA [42] replaces softmax attention with sparse attention and linear attention. While effective for scaling, pure linear attention often degrades fine-grained modeling, especially for short-range dependencies. Recent LLM studies suggest that neither full nor linear attention alone achieves the best efficiency–quality tradeoff. Hybrid designs therefore interleave linear and softmax attention to combine scalable context modeling with periodic refinement, as seen in Kimi Linear [26] and Qwen3-Next/3.5 [33, 20]. Inspired by the success of hybrid architectures in LLMs, we introduce a hybrid diffusion transformer that combines the local modeling strength of softmax attention with the global recurrent memory of linear attention for efficient, high-quality video generation.

Video Editing. Instruction-guided video editing has recently shifted from tuning-free attention manipulation and mask-based control toward large supervised video editing models. VACE [17] unifies video creation and editing through a video condition interface and context adapter. InsViE [29] and Ditto [2] emphasize scalable synthetic paired-data construction for instruction-based editing. OpenVE [14] further introduces



Figure 10 | **Causal VAE distillation.** Our decoder is comparable with the bidirectional teacher model.

OpenVE-3M and OpenVE-Bench, a unified benchmark with diverse spatially aligned and non-spatially aligned editing categories. Other recent systems, including OmniVideo [24], ICVE [19], and Lucy-Edit [25], improve instruction following and local edit fidelity through stronger multimodal conditioning, in-context learning, or open-weight video editing backbones. These methods mainly target offline short-clip editing. In contrast, SANA-Streaming focuses on real-time streaming V2V editing and achieves real-time video editing on a consumer GPU.

Long Video Generation. With the development of stronger video generation models, long video generation has attracted increasing attention. Diffusion Forcing [4], Self-Forcing [15], and Causal-Forcing [44] explore causal and autoregressive generation paradigms for producing long videos beyond the context length of pre-trained short-video generation models. Furthermore, LoL [8] studies the misbehavior of RoPE in long-video generation and proposes scaling strategies for longer temporal contexts. LongLive [34, 7] shows that causal frame-level generation, KV recaching, streaming long tuning, and short-window attention with a frame sink can enable real-time interactive long video generation. SANA-Streaming uses LongLive as the base streaming training framework and proposes cycle-reverse regularization to further improve temporal consistency.

6. Conclusion

We present SANA-Streaming, a system–algorithm co-designed framework for real-time, high-resolution streaming video-to-video editing on consumer GPUs. By combining a hybrid diffusion transformer with Cycle-Reverse Regularization and an efficient system design, our approach achieves a favorable balance between temporal consistency, visual quality, and inference efficiency under streaming constraints. Empirical results demonstrate that SANA-Streaming enables minute-length video editing at real-time speed while maintaining competitive editing quality. This work provides a practical step toward interactive video editing systems and highlights the importance of jointly addressing modeling, training, and system challenges in long-form generative tasks.

Limitations. While Cycle-Reverse Regularization mitigates the scarcity of paired data, the shortage of high-quality long video editing samples still hinders temporal consistency in complex scenarios. In addition, like other instruction-guided generative models, SANA-Streaming may produce inconsistent or incorrect edits under ambiguous or underspecified instructions. The model lacks explicit mechanisms to resolve ambiguity or guarantee faithful execution of user intent, which can lead to unpredictable outputs in challenging cases.

References

- [1] aigc apps. Videox-fun: A video generation pipeline for diffusion transformer, 2026.
- [2] Qingyan Bai, Qiuyu Wang, Hao Ouyang, Yue Yu, Hanlin Wang, Wen Wang, Ka Leong Cheng, Shuailei Ma, Yanhong Zeng, Zichen Liu, et al. Scaling instruction-based video editing with a high-quality synthetic dataset. *arXiv preprint arXiv:2510.15742*, 2025.
- [3] Pierre Charbonnier, Laure Blanc-Feraud, Gilles Aubert, and Michel Barlaud. Two deterministic half-quadratic regularization algorithms for computed imaging. In *Proceedings of 1st international conference on image processing*, volume 2, pages 168–172. IEEE, 1994.
- [4] Boyuan Chen, Diego Martí Monsó, Yilun Du, Max Simchowitz, Russ Tedrake, and Vincent Sitzmann. Diffusion forcing: Next-token prediction meets full-sequence diffusion. *Advances in Neural Information Processing Systems*, 37:24081–24125, 2024.
- [5] Junsong Chen, Shuchen Xue, Yuyang Zhao, Jincheng Yu, Sayak Paul, Junyu Chen, Han Cai, Song Han, and Enze Xie. Sana-sprint: One-step diffusion with continuous-time consistency distillation. In *Proceedings of the IEEE/CVF International Conference on Computer Vision*, pages 16185–16195, 2025.
- [6] Junsong Chen, Yuyang Zhao, Jincheng Yu, Ruihang Chu, Junyu Chen, Shuai Yang, Xianbang Wang, Yicheng Pan, Daquan Zhou, Huan Ling, et al. Sana-video: Efficient video generation with block linear diffusion transformer. *arXiv preprint arXiv:2509.24695*, 2025.
- [7] Yukang Chen, Luozhou Wang, Wei Huang, Shuai Yang, Bohan Zhang, Yicheng Xiao, Ruihang Chu, Weian Mao, Qixin Hu, Shaoteng Liu, Yuyang Zhao, Huizi Mao, Ying-Cong Chen, Enze Xie, Xiaojuan Qi, and Song Han. Longlive-2.0: An nvfp4 parallel infrastructure for long video generation, 2026.
- [8] Justin Cui, Jie Wu, Ming Li, Tao Yang, Xiaojie Li, Rui Wang, Andrew Bai, Yuanhao Ban, and Cho-Jui Hsieh. Lol: Longer than longer, scaling video generation to hour. *arXiv preprint arXiv:2601.16914*, 2026.
- [9] Tri Dao. Flashattention-2: Faster attention with better parallelism and work partitioning. *arXiv preprint arXiv:2307.08691*, 2023.
- [10] Tri Dao, Dan Fu, Stefano Ermon, Atri Rudra, and Christopher Ré. Flashattention: Fast and memory-efficient exact attention with io-awareness. *Advances in neural information processing systems*, 35:16344–16359, 2022.
- [11] Tri Dao and Albert Gu. Transformers are ssms: Generalized models and efficient algorithms through structured state space duality. *arXiv preprint arXiv:2405.21060*, 2024.
- [12] Yu Gao, Haoyuan Guo, Tuyen Hoang, Weilin Huang, Lu Jiang, Fangyuan Kong, Huixia Li, Jiashi Li, Liang Li, Xiaojie Li, et al. Seedance 1.0: Exploring the boundaries of video generation models. *arXiv preprint arXiv:2506.09113*, 2025.
- [13] Yoav HaCohen, Benny Brazowski, Nisan Chiprut, Yaki Bitterman, Andrew Kvochko, Avishai Berkowitz, Daniel Shalem, Daphna Lifschitz, Dudu Moshe, Eitan Porat, et al. Ltx-2: Efficient joint audio-visual foundation model. *arXiv preprint arXiv:2601.03233*, 2026.
- [14] Haoyang He, Jie Wang, Jiangning Zhang, Zhucun Xue, Xingyuan Bu, Qiangpeng Yang, Shilei Wen, and Lei Xie. Openve-3m: A large-scale high-quality dataset for instruction-guided video editing. *arXiv preprint arXiv:2512.07826*, 2025.
- [15] Xun Huang, Zhengqi Li, Guande He, Mingyuan Zhou, and Eli Shechtman. Self forcing: Bridging the train-test gap in autoregressive video diffusion. *arXiv preprint arXiv:2506.08009*, 2025.
- [16] Hakan Inan, Kartikeya Upasani, Jianfeng Chi, Rashi Rungta, Krithika Iyer, Yuning Mao, Michael Tontchev, Qing Hu, Brian Fuller, Davide Testuggine, et al. Llama guard: Llm-based input-output safeguard for human-ai conversations. *arXiv preprint arXiv:2312.06674*, 2023.
- [17] Zeyinzi Jiang, Zhen Han, Chaojie Mao, Jingfeng Zhang, Yulin Pan, and Yu Liu. Vace: All-in-one video creation and editing. In *Proceedings of the IEEE/CVF International Conference on Computer Vision*, pages 17191–17202, 2025.

- [18] Justin Johnson, Alexandre Alahi, and Li Fei-Fei. Perceptual losses for real-time style transfer and super-resolution. In *European conference on computer vision*, pages 694–711. Springer, 2016.
- [19] Xinyao Liao, Xianfang Zeng, Ziyi Song, Zhoujie Fu, Gang Yu, and Guosheng Lin. In-context learning with unpaired clips for instruction-based video editing. *arXiv preprint arXiv:2510.14648*, 2025.
- [20] Qwen Team. Qwen3.5: Towards native multimodal agents, February 2026.
- [21] Imanol Schlag, Kazuki Irie, and Jürgen Schmidhuber. Linear transformers are secretly fast weight programmers. In *International conference on machine learning*, pages 9355–9366. PMLR, 2021.
- [22] Jianlin Su, Yu Lu, Shengfeng Pan, Ahmed Murtadha, Bo Wen, and Yunfeng Liu. Roformer: Enhanced transformer with rotary position embedding. *arXiv preprint arXiv:2104.09864*, 2021.
- [23] Yutao Sun, Li Dong, Shaohan Huang, Shuming Ma, Yuqing Xia, Jilong Xue, Jianyong Wang, and Furu Wei. Retentive network: A successor to transformer for large language models. *arXiv preprint arXiv:2307.08621*, 2023.
- [24] Zhiyu Tan, Hao Yang, Luozheng Qin, Jia Gong, Mengping Yang, and Hao Li. Omni-video: Democratizing unified video understanding and generation. *arXiv preprint arXiv:2507.06119*, 2025.
- [25] DecartAI Team. Lucy edit: Open-weight text-guided video editing. 2025.
- [26] Kimi Team, Yu Zhang, Zongyu Lin, Xingcheng Yao, Jiayi Hu, Fanqing Meng, Chengyin Liu, Xin Men, Songlin Yang, Zhiyuan Li, et al. Kimi linear: An expressive, efficient attention architecture. *arXiv preprint arXiv:2510.26692*, 2025.
- [27] Team Wan, Ang Wang, Baole Ai, Bin Wen, Chaojie Mao, Chen-Wei Xie, Di Chen, Feiwei Yu, Haiming Zhao, Jianxiao Yang, et al. Wan: Open and advanced large-scale video generative models. *arXiv preprint arXiv:2503.20314*, 2025.
- [28] Chenfei Wu, Jiahao Li, Jingren Zhou, Junyang Lin, Kaiyuan Gao, Kun Yan, Sheng-ming Yin, Shuai Bai, Xiao Xu, Yilei Chen, et al. Qwen-image technical report. *arXiv preprint arXiv:2508.02324*, 2025.
- [29] Yuhui Wu, Liyi Chen, Ruibin Li, Shihao Wang, Chenxi Xie, and Lei Zhang. Insvie-1m: Effective instruction-based video editing with elaborate dataset construction. In *Proceedings of the IEEE/CVF International Conference on Computer Vision*, pages 16692–16701, 2025.
- [30] Guangxuan Xiao, Yuandong Tian, Beidi Chen, Song Han, and Mike Lewis. Efficient streaming language models with attention sinks. *arXiv preprint arXiv:2309.17453*, 2023.
- [31] Enze Xie, Junsong Chen, Junyu Chen, Han Cai, Haotian Tang, Yujun Lin, Zhekai Zhang, Muyang Li, Ligeng Zhu, Yao Lu, et al. Sana: Efficient high-resolution image synthesis with linear diffusion transformers. *arXiv preprint arXiv:2410.10629*, 2024.
- [32] Enze Xie, Junsong Chen, Yuyang Zhao, Jincheng Yu, Ligeng Zhu, Chengyue Wu, Yujun Lin, Zhekai Zhang, Muyang Li, Junyu Chen, et al. Sana 1.5: Efficient scaling of training-time and inference-time compute in linear diffusion transformer. *arXiv preprint arXiv:2501.18427*, 2025.
- [33] An Yang, Anfeng Li, Baosong Yang, Beichen Zhang, Binyuan Hui, Bo Zheng, Bowen Yu, Chang Gao, Chengen Huang, Chenxu Lv, et al. Qwen3 technical report. *arXiv preprint arXiv:2505.09388*, 2025.
- [34] Shuai Yang, Wei Huang, Ruihang Chu, Yicheng Xiao, Yuyang Zhao, Xianbang Wang, Muyang Li, Enze Xie, Yingcong Chen, Yao Lu, et al. Longlive: Real-time interactive long video generation. *arXiv preprint arXiv:2509.22622*, 2025.
- [35] Songlin Yang, Jan Kautz, and Ali Hatamizadeh. Gated delta networks: Improving mamba2 with delta rule. *arXiv preprint arXiv:2412.06464*, 2024.
- [36] Songlin Yang, Bailin Wang, Yikang Shen, Rameswar Panda, and Yoon Kim. Gated linear attention transformers with hardware-efficient training. *arXiv preprint arXiv:2312.06635*, 2023.

- [37] Tian Ye, Song Fei, and Lei Zhu. Ultraflux: Data-model co-design for high-quality native 4k text-to-image generation across diverse aspect ratios. *arXiv preprint arXiv:2511.18050*, 2025.
- [38] Tianwei Yin, Michaël Gharbi, Taesung Park, Richard Zhang, Eli Shechtman, Fredo Durand, and William T Freeman. Improved distribution matching distillation for fast image synthesis. *Advances in neural information processing systems*, 37:47455–47487, 2024.
- [39] Tianwei Yin, Michaël Gharbi, Richard Zhang, Eli Shechtman, Fredo Durand, William T Freeman, and Taesung Park. One-step diffusion with distribution matching distillation. In *Proceedings of the IEEE/CVF conference on computer vision and pattern recognition*, pages 6613–6623, 2024.
- [40] Biao Zhang and Rico Sennrich. Root mean square layer normalization. *Advances in neural information processing systems*, 32, 2019.
- [41] Jinjin Zhang, Qiuyu Huang, Junjie Liu, Xiefan Guo, and Di Huang. Diffusion-4k: Ultra-high-resolution image synthesis with latent diffusion models. In *Proceedings of the Computer Vision and Pattern Recognition Conference*, pages 23464–23473, 2025.
- [42] Jintao Zhang, Haoxu Wang, Kai Jiang, Shuo Yang, Kaiwen Zheng, Haocheng Xi, Ziteng Wang, Hongzhou Zhu, Min Zhao, Ion Stoica, et al. Sla: Beyond sparsity in diffusion transformers via fine-tunable sparse-linear attention. *arXiv preprint arXiv:2509.24006*, 2025.
- [43] Haoyi Zhu, Haozhe Liu, Yuyang Zhao, Tian Ye, Junsong Chen, Jincheng Yu, Tong He, Song Han, and Enze Xie. Sana-wm: Efficient minute-scale world modeling with hybrid linear diffusion transformer. *arXiv preprint arXiv:2605.15178*, 2026.
- [44] Hongzhou Zhu, Min Zhao, Guande He, Hang Su, Chongxuan Li, and Jun Zhu. Causal forcing: Autoregressive diffusion distillation done right for high-quality real-time interactive video generation. *arXiv preprint arXiv:2602.02214*, 2026.
- [45] Ya Zou, Jingfeng Yao, Siyuan Yu, Shuai Zhang, Wenyu Liu, and Xinggang Wang. Turbo-vaed: Fast and stable transfer of video-vaes to mobile devices. In *Proceedings of the AAAI Conference on Artificial Intelligence*, 2026.

A. Mixed-Precision Quantization

Search setup and metrics. *Quality.* For each candidate policy, we run the full 30-second streaming generation under the same input noise as the BF16 reference on 45 calibration prompts, and compare the produced output latent against the BF16 output latent. We report the relative RMSE and LPIPS averaged over the calibration set (lower is better), where RelRMSE normalizes the latent RMSE by the BF16 reference’s standard deviation so that errors are comparable across prompts of different scale. *Compute accounting.* The DiT processes the 30-second video in chunks of 3 latent frames, so a single forward pass operates on a chunk of $3 \times 22 \times 40$ latent tokens. The FLOP totals in Table 4 are for this single per-chunk forward, computed as $\sum_{\ell} 2 \cdot \text{in}_{\ell} \cdot \text{out}_{\ell} \cdot N_{\ell}$ over every quantizable linear / point-wise convolution, with N_{ℓ} the tokens seen by layer ℓ ($N = 2640$ for self-attention and FFN, $N = 300$ for cross-attention key/value over text tokens). The full DiT then executes ~ 9.84 T FLOPs per chunk; reporting per-chunk FLOPs (rather than per-video) is sufficient because the FP4 / FP8 fractions and the resulting speedup factors are invariant to the chunk count. *Columns.* *#Params FP4* and *FLOPs* are the parameters (M) and per-chunk FLOPs (G) demoted to FP4 in each configuration; the remaining linear layers stay in FP8. *%Param / %FLOPs* are the corresponding shares of the full DiT. *Speedup* is the idealized roofline factor over BF16, so all-FP8 gives 2x and all-FP4 gives 4x. To collapse quality and efficiency into a single scalar, we report *Cost over Speedup* = RMSE/Speedup: the FP8 ratio of 0.23 is the reference that guides us to identify the best mixed-precision policy.

Table 4 | Mixed-precision search summary on the SANA hybrid DiT (2B parameters, 9.84 T FLOPs in a chunk generation of $3 \times 22 \times 40$ latent).

Config / module	#Params FP4 (M)	FLOPs (G)	%Param	%FLOPs	RMSE ↓	LPIPS ↓	Speedup ↑	Cost over Speedup ↓
<i>Baselines</i>								
FP8	0	0	0%	0%	0.45	0.10	2.00×	0.23
FP4	2040	9840	100%	100%	1.04	0.35	4.00×	0.26
<i>Single-group FP4 (only this group → FP4, rest FP8)</i>								
FFN-Input	602	3179	29%	32%	0.65	0.17	2.39×	0.27
FFN-Output	310	1635	15%	17%	0.57	0.14	2.18×	0.26
FFN-Temporal	310	1635	15%	17%	0.52	0.12	2.18×	0.24
SA-O	103	545	5%	6%	0.61	0.15	2.06×	0.30
SA-Q	103	545	5%	6%	0.47	0.10	2.06×	0.23
SA-K	103	545	5%	6%	0.49	0.11	2.06×	0.24
SA-V	103	545	5%	6%	0.56	0.13	2.06×	0.27
CA-Q	103	545	5%	6%	0.54	0.12	2.06×	0.26
CA-O	103	545	5%	6%	0.46	0.10	2.06×	0.22
CA-KV	201	120	10%	1%	0.49	0.11	2.01×	0.24
<i>Block-range FP4 (all modules in this block range → FP4)</i>								
Shallow Blocks (0-5)	612	2950	30%	30%	0.79	0.22	2.35×	0.34
Middle Blocks (6-13)	816	3940	40%	40%	0.71	0.19	2.50×	0.29
Deep Blocks (14-19)	612	2950	30%	30%	0.64	0.16	2.35×	0.27
<i>Mixed-Precision</i>								
Basic Mix (CA-O + SA-Q + SA-K + FFN-Temporal)	619	3270	30%	33%	0.56	0.14	2.40×	0.23
Basic Mix + FFN-Input/Output (Deep blocks 14-19)	893	4710	44%	48%	0.60	0.15	2.63×	0.23
Basic Mix + FFN-Input/Output (Deep+Mid 6-19, Ours)	1258	6640	62%	67%	0.64	0.17	3.02×	0.21

Trade-off analysis. We make the following observations from Table 4. **First**, the baselines reveal the central tension: pure FP4 has a higher cost over speedup than FP8 (0.26 vs. 0.23), so doubling the raw compute speedup does not pay back the quality penalty. The goal of the search is therefore not to push as much as possible to FP4, but to find a mixed policy whose ratio is strictly below the FP8 reference of 0.23. **Second**, the single-group sweep spreads from 0.22 (CA-O) to 0.30 (SA-O), and only CA-O dips below the FP8 reference on its own; SA-Q, SA-K and FFN-Temporal sit just above, while the value/post-mixing projections (SA-V, SA-O, CA-Q) and FFN input/output project clearly above FP8, providing direct evidence for the per-layer decisions made above. **Third**, holding the FP4 FLOP budget fixed at 30% across the three block ranges flips the cost-over-speedup ratio from 0.34 (shallow) through 0.29 (middle) to 0.27 (deep): the same FP4 budget hurts least when spent on the deeper blocks, motivating the depth-restricted demotion of FFN input/output. **Finally**, the build-up in the mixed-precision section makes the trade-off concrete: Basic Mix matches the FP8 ratio (0.23 at 2.40×); adding FFN input/output in the deep blocks holds the ratio at 0.23 while lifting the speedup to 2.63×; and only extending those FFN demotions into the middle blocks (*Ours*) drops the ratio below FP8, reaching 0.21 at an idealized 3.02× speedup over BF16, dominating both baselines and every intermediate configuration we evaluated.

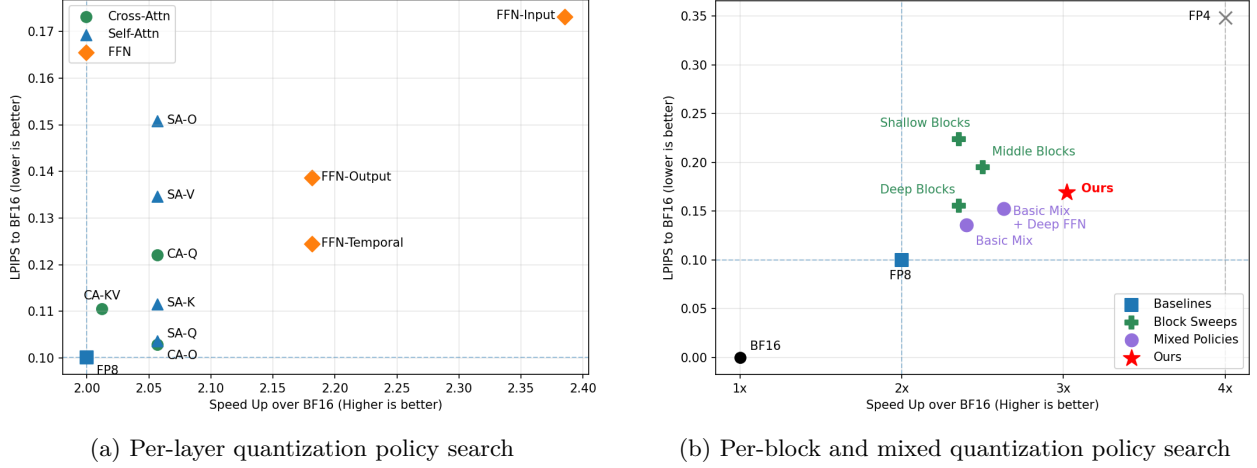


Figure 11 | **Mixed-Precision Quantization Policy Search on LPIPS.** For each subfigure, the x-axis is the estimated speed up and the y-axis is the quantization error over the BF16 reference. The selected mixed-precision policy achieves the best trade-off between efficiency and quality.



Figure 12 | **Limitations of Linear Attention.** Purely linear attention [6] suffers from visible chunk-to-chunk appearance jumps and temporal flicker.

B. Implementation Details

Model Design. SANA-Streaming is a 2B hybrid diffusion transformer with the LTX2 VAE [13] (compression ratio $32 \times 32 \times 8$). The DiT contains 20 transformer blocks, including 5 evenly inserted softmax-attention blocks and 15 GDN blocks. The hidden size is 2240 with 20 attention heads.

Dataset. We use the open-source Ditto [2] and OpenVE [14] datasets, as well as the human-centric editing data built by our data pipeline (Appendix E). The total number of short video clips is about 10M. For the pretraining stage, we filter the dataset based on our VLM verification results, with dataset-specific filtering criteria, obtaining 7M clips after filtering. In the SFT stage, we use stricter filtering criteria to obtain 1M clips. For the long-video dataset, we use an internal dataset with 10K one-minute videos and annotate the edit instruction and reverse instruction using our data pipeline.

Model Training. The bidirectional model is trained with 32 NVIDIA H100 GPUs for about 100K iterations with batch size 2 per GPU. The learning rate is set to $5e-5$ with the AdamW optimizer. For the long training stage, following LongLive [34], we train the model in three stages: ODE initialization, self-forcing training, and streaming long training. The proposed cycle-reverse regularization is adopted in the long training stage.

Algorithm 1 Bidirectional GDN forward

Require: $qkv \in \mathbb{R}^{B \times FS \times 3 \times H \times D}$, β , decay α , normalization weights, RoPE tables

Ensure: output $O \in \mathbb{R}^{B \times FS \times H \times D}$

```

1: Pad head dimension to BLOCK_D = 128                                     ▷ Phase A: frame-parallel summaries
2: for all  $(b, h, f)$  in parallel do
3:    $P_f \leftarrow I - K_{\text{rot},f}^\top \text{diag}(\beta_f) K_{\text{rot},f}$ 
4:    $A_f \leftarrow K_{\text{rot},f}^\top \text{diag}(\beta_f) V_f$ 
5:    $P_f^z \leftarrow I - K_f^\top \text{diag}(\beta_f) K_f$ 
6:    $b_f \leftarrow K_f^\top \beta_f$ 
7: end for                                                                 ▷ Phase B: compact recurrent scans
8: for all  $(b, h)$  in parallel do
9:    $S_{-1}^\rightarrow, z_{-1}^\rightarrow \leftarrow$  cached state or zero
10:  for  $f = 0$  to  $F - 1$  do
11:     $S_f^\rightarrow \leftarrow \alpha_f P_f S_{f-1}^\rightarrow + A_f$ 
12:     $z_f^\rightarrow \leftarrow \alpha_f P_f^z z_{f-1}^\rightarrow + b_f$ 
13:  end for
14:   $S_{F-1}^\leftarrow, z_{F-1}^\leftarrow \leftarrow 0$ 
15:  for  $f = F - 1$  down to 1 do
16:     $S_{f-1}^\leftarrow \leftarrow \alpha_f P_f S_f^\leftarrow + A_f$ 
17:     $z_{f-1}^\leftarrow \leftarrow \alpha_f P_f^z z_f^\leftarrow + b_f$ 
18:  end for
19:  for  $f = 0$  to  $F - 1$  do
20:     $S_f^{\text{hist}} \leftarrow S_f^\rightarrow + S_f^\leftarrow$ 
21:     $z_f^{\text{hist}} \leftarrow z_f^\rightarrow + z_f^\leftarrow$ 
22:  end for
23: end for                                                                 ▷ Phase C: output streaming over spatial tiles
24: for all  $(b, h, f)$  in parallel do
25:   for  $s_0 = 0$  to  $S - 1$  step BLOCK_S do
26:    Load and normalize  $Q_{f,s_0:s_0+\text{BLOCK}_S}$ 
27:    Apply RoPE to obtain  $Q_{\text{rot}}$ 
28:     $N \leftarrow Q_{\text{rot}} S_f^{\text{hist}}$ 
29:     $d \leftarrow Q z_f^{\text{hist}}$ 
30:     $O_{f,s_0:s_0+\text{BLOCK}_S} \leftarrow N / (d + \epsilon)$ 
31:   end for
32: end for
    
```

C. More Results

We present additional video editing results in Figure 13. For each group, the first row shows the original video as the source reference. The subsequent rows demonstrate our model’s capability in three distinct editing tasks: style transfer (e.g., low poly or mosaic), background replacement (e.g., concrete terrace or boxing gym), and local object addition (e.g., adding a lantern or dragonfly). The results show that our method can precisely apply these modifications while maintaining high temporal consistency and structural fidelity to the original motion and character identity. Figure 12 further illustrates the chunk-boundary artifacts of pure linear attention, motivating the hybrid architecture used in SANA-Streaming.

D. GDN Kernel Details

Tensor shapes and layout. This appendix describes the Triton GDN kernel used in our experiments. The input layout is $qkv \in \mathbb{R}^{B \times N \times 3 \times H \times D}$ with $N = FS$. In the production configuration, $D = 112$ is padded to $\text{BLOCK}_D=128$ inside the kernels. The recurrent matrix state therefore has shape 128×128 per (B, H) stream, and the vector state has length 128. Intermediate frame summaries use shape $(BH, F, 128, 128)$ for matrix terms and $(BH, F, 128)$ for vector terms.

GPU	precision	Phase A (nw, BS)	Phase B (d, nw, ns, acc)	Phase C (nw, BS)
A100	fp32	(16, 32)	(4, 32, 1, +)	(16, 32)
A100	TF32	(16, 32)	(4, 8, 2, -)	(16, 32)
A100	bf16	(8, 32)	(4, 8, 2, -)	(4, 32)
H100	fp32	(8, 32)	(4, 32, 1, +)	(16, 32)
H100	TF32	(8, 32)	(4, 8, 2, -)	(16, 32)
H100	bf16	(8, 64)	(4, 8, 2, -)	(8, 32)
GB200	fp32	(8, 128)	(8, 4, 1, -)	(4, 64)
GB200	TF32	(8, 128)	(4, 8, 2, -)	(4, 64)
GB200	bf16	(4, 64)	(4, 8, 2, -)	(8, 64)
5090	fp32	(8, 16)	(8, 4, 1, -)	(8, 16)
5090	TF32	(8, 16)	(8, 8, 1, -)	(8, 16)
5090	bf16	(8, 32)	(8, 8, 1, -)	(4, 32)
GB10	fp32	(8, 16)	(8, 4, 1, -)	(8, 16)
GB10	TF32	(8, 16)	(1, 8, 1, -)	(8, 16)
GB10	bf16	(8, 32)	(1, 8, 1, -)	(4, 32)

Table 5 | Final Triton launch parameters. Across phases, nw is the number of warps, ns is the number of pipeline stages, and BS is the spatial block size. For Phase B, d is the number of output-column splits ($d = 1$ means no D-tiling), and acc indicates whether accumulator fusion is enabled.

Implementation details. Phase A is implemented as two kernels: a matrix stream for (P_f, A_f) and a lighter vector stream for (P_f^z, b_f) . The vector stream does not need V or RoPE. Both streams accumulate frame summaries in fp32 and store $I - P$ directly, so Phase B can compute $(I - P)S$ with one MMA. Phase B keeps the scan state in fp32. In bidirectional mode it writes the reverse contribution directly into the forward history buffer, so Phase C is launched once on the combined history. Phase C then streams the spatial dimension of Q_f in BLOCK_S tiles.

Precision modes. The kernel supports three dot-product modes, inherited from the global GDN precision setting:

- **fp32:** Triton dot operands are fp32 with `input_precision="ieee"`. The Phase-A to Phase-B HBM bridge is fp32, and Phase-C numerator/denominator buffers are fp32.
- **TF32:** the Phase-A to Phase-B bridge remains fp32, but matrix products use TF32 tensor cores.
- **bf16:** dot operands use bf16 tensor cores with fp32 accumulation. Phase-A summaries and Phase-C output buffers are stored in bf16 to reduce HBM traffic, while the recurrent Phase-B scan state remains fp32.

For fp32 and TF32 modes, the frame summaries communicated between Phase A and Phase B are stored in fp32. For bf16 mode, they are stored in bf16 to reduce HBM traffic.

Architecture-specific launch parameters. We tune Phase A, B, and C separately because they stress different resources. Phase A and C are spatial streaming kernels controlled mainly by BLOCK_S. Phase B is a compact recurrent scan controlled mainly by the number of warps and whether D-tiling is enabled. fp32 and TF32 share the same Phase-A and Phase-C launch shapes, but Phase B is dispatched by the exact dot-product mode. Table 5 shows the final effective launch configuration used by the kernel.

D-tiled Phase B. For Phase B, the output columns of the matrix recurrence are independent:

$$S_f[:, J] = \alpha_f P_f S_{f-1}[:, J] + A_f[:, J].$$

We exploit this by splitting the output-column dimension into d_{splits} tiles. Each Triton program owns one column tile J , which lowers live state size and increases grid parallelism. The vector state z_f is not column-splittable, so only the leading D-tile computes it. Because D-tiling also duplicates reads of P_f , the selected policy depends on GPU and precision, as shown in Table 5.

GPU	precision	impl.	fixed			sink			rolling			
			total (s)	ch0 (ms)	ch1+ (ms)	total (s)	ch0 (ms)	ch1+ (ms)	total (s)	ch0 (ms)	ch1+ (ms)	
A100	fp32	PyTorch	232.69	72.30	67.15	237.52	75.77	69.98	252.31	72.78	79.45	
		Kernel	87.72 (2.65×)	7.20 (10.04×)	4.87 (13.78×)	94.26 (2.52×)	13.04 (5.81×)	10.47 (6.68×)	99.30 (2.54×)	12.96 (5.61×)	14.37 (5.53×)	
	bf16	PyTorch	57.50	12.07	7.85	60.63	12.08	8.85	69.51	12.32	13.90	
		Kernel	43.03 (1.34×)	3.45 (3.49×)	2.47 (3.18×)	46.07 (1.32×)	4.02 (3.01×)	3.74 (2.36×)	48.40 (1.44×)	3.99 (3.08×)	4.99 (2.78×)	
	H100	fp32	PyTorch	32.35	9.35	5.99	35.02	9.33	7.53	43.88	9.61	13.20
			Kernel	21.69 (1.49×)	6.06 (1.54×)	2.88 (2.08×)	24.62 (1.42×)	5.78 (1.61×)	5.24 (1.44×)	27.72 (1.58×)	3.84 (2.50×)	5.58 (2.37×)
bf16		PyTorch	28.86	7.23	4.73	30.89	7.18	5.26	36.36	7.40	8.43	
		Kernel	18.88 (1.53×)	1.58 (4.56×)	1.05 (4.49×)	20.86 (1.48×)	1.94 (3.71×)	1.71 (3.09×)	22.19 (1.64×)	1.92 (3.85×)	2.61 (3.23×)	
GB200		fp32	PyTorch	21.65	6.44	4.54	23.30	6.34	5.27	30.46	6.70	9.96
			Kernel	13.71 (1.58×)	2.40 (2.68×)	1.55 (2.93×)	15.40 (1.51×)	2.50 (2.54×)	2.53 (2.08×)	16.94 (1.80×)	2.53 (2.65×)	3.51 (2.84×)
	bf16	PyTorch	22.32	6.21	4.55	23.51	6.19	5.37	30.84	6.23	9.12	
		Kernel	13.65 (1.64×)	1.41 (4.42×)	1.51 (3.02×)	15.52 (1.51×)	1.54 (4.02×)	2.33 (2.30×)	15.43 (2.00×)	1.48 (4.21×)	2.22 (4.10×)	
	5090	fp32	PyTorch	89.28	11.40	24.74	92.59	11.43	26.86	103.43	11.72	33.21
			Kernel	49.16 (1.82×)	5.08 (2.24×)	2.95 (8.39×)	51.73 (1.79×)	5.30 (2.16×)	4.54 (5.92×)	53.13 (1.95×)	4.23 (2.77×)	4.98 (6.67×)
bf16		PyTorch	46.03	9.39	5.72	47.17	9.08	6.55	55.17	9.56	10.51	
		Kernel	35.83 (1.28×)	3.20 (2.94×)	2.11 (2.71×)	36.59 (1.29×)	3.48 (2.61×)	2.60 (2.52×)	39.72 (1.39×)	3.59 (2.66×)	3.74 (2.81×)	
GB10		fp32	PyTorch	397.58	117.57	93.70	425.10	117.94	107.12	491.71	120.16	149.10
			Kernel	193.76 (2.05×)	16.55 (7.10×)	10.02 (9.35×)	212.71 (2.00×)	18.25 (6.46×)	18.11 (5.92×)	229.11 (2.15×)	18.34 (6.55×)	26.87 (5.55×)
	bf16	PyTorch	368.64	101.09	83.62	393.57	101.44	91.01	434.69	102.39	116.46	
		Kernel	186.15 (1.98×)	12.48 (8.10×)	7.88 (10.62×)	206.15 (1.91×)	15.83 (6.41×)	13.47 (6.75×)	216.68 (2.01×)	15.77 (6.49×)	19.81 (5.88×)	

Table 6 | GDN-kernel runtimes and speedups over PyTorch. PyTorch rows report baseline runtimes; Kernel rows report Triton-kernel runtimes with speedup in parentheses. Column headers give units: *total* is end-to-end sampling time in seconds, while *ch0* and *ch1+* are per-call GDN times in milliseconds for the first chunk and later chunks, respectively. The three RoPE/cache strategies are fixed-RoPE, rolling-RoPE with sink, and rolling-RoPE.

Benchmark. We evaluate three RoPE/cache strategies: fixed-RoPE, rolling-RoPE with sink, and rolling-RoPE. All runs use the same output chunk pattern, with an initial five-frame chunk followed by three-frame chunks. In Table 6, *total* is the end-to-end sampling time, *ch0* is the first GDN call that emits five frames, and *ch1+* is the median subsequent GDN call that emits three frames. Depending on the cache strategy, a GDN call may also consume cached recurrent state or replay cached pre-RoPE context internally. We report two measurements. First, the end-to-end sampling time is the wall-clock time of the diffusion sampling phase; video preparation, VAE decoding, encoding, and saving are excluded. Second, per-call GDN time is measured inside the model with CUDA events around each GDN forward call. Calls are bucketed by strategy and chunk type, and we report the median time for the initial chunk (*ch0*) and the subsequent chunks (*ch1+*). For each configuration we run PyTorch and the Triton GDN kernel under the same precision setting and compute speedup as the ratio of PyTorch time to Triton-kernel time. The reported sampling time uses the second generated sample to avoid one-time warmup effects. Table 6 reports PyTorch and Triton-kernel runtimes, with speedups over PyTorch in parentheses on the Triton rows. In fp32, per-call GDN speedups are 1.4×–13.8× across five GPU classes and three rope strategies; end-to-end sampling speedups are 1.42×–2.65× because non-GDN work remains in the pipeline. At bf16, per-call speedups are 2.3×–10.6× and sampling speedups are 1.28×–2.01×.

E. Data Pipeline

Our data pipeline aims to construct high-quality human-centric video editing pairs, enabling controllable semantic edits and temporally coherent motion. In the following subsections, we present the construction process for both short and long videos, along with the corresponding quality control procedures. Figure 7 summarizes the complete pipeline, including short-video pair construction, long-video instruction construction, and VLM-based filtering.

E.1. Short Video

Edit Instruction Generation and First Frame Edit. We first generate edit instructions with a taxonomy-guided prompting strategy. For each source video, we sample an editing task from four high-level categories: local human edits, background edits, artistic style transfer, and composite edits. *Local edits* include outfit replacement, outfit color or pattern changes, hairstyle changes, hair color changes, and accessory edits. *Background edits* either replace the scene while preserving the subject, or jointly adapt the background and outfit to form a coherent contextual transformation. *Style-transfer* instructions are sampled from a diverse style dictionary, while *composite edits* combine multiple attributes such as fashion, hair, makeup, setting, season, decade, or character archetype. Given the sampled task, we prompt a vision-language model, Qwen3VL [33], to analyze the source video and produce a single self-contained editing instruction with concrete visual details such as material, color, silhouette, texture, lighting interaction, and style coherence. We then apply this edit to the first frame of the video. Specifically, we use Qwen-Image-Edit [28] conditioned on the edit instruction, the first frame, and the pose extracted from the first frame to obtain an edited first frame, which serves as a visual anchor for later edit-video generation.

In-Context Generation for Edit Video. To enable fine-grained and controllable video editing, we provide the edited first frame and the source video to Qwen3VL [33] to generate a caption describing the desired target video content. Meanwhile, we extract a pose video from the source video to serve as a motion anchor, preserving temporal dynamics. Conditioned on these signals, we generate the edited video using a controllable text-image-video-to-video pipeline, Wan2.2-Fun-Control [1]. For each sample, the generated caption serves as the text prompt, the pose video provides motion guidance, and the edited first frame is used as both the initial frame and a visual reference.

E.2. Long Video

To support streaming long training and cycle-reverse regularization, we construct an additional long-video subset with paired forward and backward edit instructions. For each long source video, we first sample a representative anchor frame, typically the first frame, and use it as the visual evidence for instruction generation. Conditioned on the anchor frame, we use Gemini-3-Flash to generate the forward edit instruction p^+ . The edit prompt is sampled from five edit families: background replacement, local addition, local removal, local replacement, and style transfer, following the taxonomy-based approach described above.

We construct the backward instruction p^- using the source video and its forward instruction p^+ . The VLM is asked to infer the inverse operation that would recover the observed source content after the forward edit has been applied.

E.3. Data Verification

VLM Verification for Short Video. After generating candidate edited videos, we apply VLM-based verification to filter low-quality samples. The verifier compares each edited video against the original source video, the edit instruction, and the predicted edited-video caption. This comparison is necessary because a generated video can be visually plausible while still failing to follow the intended edit, altering non-edit regions, or introducing temporal artifacts.

We evaluate each candidate along four dimensions. *Instruction alignment* measures whether the edited video faithfully implements the requested semantic change. *Non-edit consistency and temporal stability* measures whether regions not targeted by the edit are preserved from the source video and whether the output remains stable across frames. *Physical plausibility* evaluates lighting consistency, geometry, motion, and other real-world constraints after editing. *Video quality* captures sharpness, color stability, compression artifacts,

and overall visual coherence. Each dimension is scored on a 0–10 scale, and the verifier also returns brief comments describing strengths and failure cases. The resulting scores and textual comments are saved for each sample and used to select the final training data.

Data Verification and VLM Verification for Long Videos. Long videos may contain title cards or black-screen segments that provide little useful editing content. We sample the first and last 10 seconds at approximately 2 FPS, and discard videos with excessive near-black pixel ratio. Moreover, for long-video self-forcing distillation, the student is bounded by the teacher’s editing capability; if the teacher cannot execute a forward edit, the corresponding long sample provides little useful supervision. We therefore verify long-video instructions by taking the first 81 frames of each source video and asking the teacher model to generate the edited 81-frame clip conditioned on the forward instruction. A VLM then compares the source clip, the teacher-edited clip, and the instruction, deciding whether the specified edit is successfully performed. If not, we discard the sample.

F. Causal VAE Training

We train only the decoder of the causal VAE, while keeping the pretrained VAE encoder fixed. Given a training video $x \in \mathbb{R}^{B \times C \times T \times H \times W}$, the frozen encoder produces a latent code z , and the causal decoder reconstructs $\hat{x} = D_\theta^{\text{causal}}(z)$. The bidirectional LTX2 decoder is used as a frozen teacher for intermediate feature supervision. Below we expand the loss terms in Eq. 3. For compact notation, $x_{b,t}$ and $\hat{x}_{b,t}$ denote the t -th frame of the target and reconstruction in video b .

Charbonnier reconstruction loss. For robust pixel-level reconstruction, we use a Charbonnier penalty on the decoded video:

$$\mathcal{L}_{\text{charb}} = \frac{1}{BCTHW} \sum_{b,c,t,h,w} \sqrt{(\hat{x}_{b,c,t,h,w} - x_{b,c,t,h,w})^2 + \epsilon^2}, \quad \epsilon = 10^{-6}. \quad (7)$$

This term behaves similarly to an ℓ_1 reconstruction loss for large residuals while remaining smooth around zero, which stabilizes decoder-only fine-tuning.

Perceptual loss. To preserve perceptual similarity beyond per-pixel accuracy, we apply the AlexNet-based LPIPS loss independently to each video frame:

$$\mathcal{L}_{\text{perc}} = \frac{1}{BT} \sum_{b,t} \mathcal{D}_{\text{LPIPS}}^{\text{Alex}}(\hat{x}_{b,t}, x_{b,t}). \quad (8)$$

Haar wavelet loss. The Haar wavelet term explicitly supervises high-frequency details. Let $\mathcal{W}_H(\cdot)$ denote a single-level 2D Haar transform applied frame by frame, and let $\mathcal{W}_H^{\text{high}}(\cdot)$ concatenate the three high-frequency subbands LH, HL, and HH, omitting the low-frequency LL band. We minimize

$$\mathcal{L}_{\text{haar}} = \frac{1}{BT} \sum_{b,t} \frac{1}{M_H} \left\| \mathcal{W}_H^{\text{high}}(\hat{x}_{b,t}) - \mathcal{W}_H^{\text{high}}(x_{b,t}) \right\|_1. \quad (9)$$

Here M_H is the number of high-frequency Haar coefficients per frame. This loss encourages the causal decoder to recover sharp edges and fine texture that are often smoothed by purely pixel-level objectives.

Intermediate feature distillation. We further align the causal student decoder with the bidirectional teacher decoder using intermediate activations. Let $F_\ell^S(z)$ and $F_\ell^T(z)$ be the student and teacher decoder features at layer ℓ , where ℓ is selected from the decoder mid-block and upsampling blocks. The teacher is frozen and gradients are stopped through its features:

$$\mathcal{L}_{\text{distill}} = \sum_{\ell \in \mathcal{S}} \frac{1}{N_\ell} \|F_\ell^S(z) - F_\ell^T(z)\|_2^2, \quad (10)$$

where \mathcal{S} is the set of distilled decoder blocks and N_ℓ is the number of elements in the feature tensor.

G. Frame-wise Gated DeltaNet

This section provides the detailed formulation of the frame-wise Gated DeltaNet (GDN) block used in SANA-Streaming, which extends the Gated Delta Network [35] to the frame-wise streaming video setting. The design goal of this block is to provide a compact, finite recurrent memory for causal streaming generation: instead of caching raw key/value tokens from all previous chunks, each GDN block only carries forward the terminal recurrent states from the previous chunk, so the cache size is independent of the number of streamed chunks.

G.1. Notation

All equations below are presented for a single attention head; the full multi-head computation runs H heads in parallel and concatenates their outputs along the channel dimension. For a chunk of F frames with N spatial tokens per frame, the per-head latent feature is

$$x \in \mathbb{R}^{F \times N \times D},$$

where D is the per-head channel dimension. For the f -th frame, the per-head input tokens are

$$x_f \in \mathbb{R}^{N \times D}.$$

For convenience we use the column-token convention in the following derivation,

$$X_f = x_f^\top \in \mathbb{R}^{D \times N},$$

and we omit the head index h throughout, with the understanding that all weight matrices are head-specific. Each head maintains two recurrent states: a KV memory

$$S_f^{kv} \in \mathbb{R}^{D \times D}$$

and a normalizer state

$$S_f^z \in \mathbb{R}^D.$$

G.2. Feature parameterization

Given X_f , the block computes per-head query, key, and value features by pointwise (kernel size 1) linear projections:

$$Q_f = W_q X_f, \quad K_f = W_k X_f, \quad V_f = W_v X_f, \quad (11)$$

where $W_q, W_k, W_v \in \mathbb{R}^{D \times D}$ and $Q_f, K_f, V_f \in \mathbb{R}^{D \times N}$. We then apply RMSNorm [40], a ReLU kernel feature map following Sana’s linear attention design [31], and a fixed 3D RoPE [22] to the query and key:

$$\hat{Q}_f = \rho_{3D} \left(\text{ReLU}(\text{RMSNorm}(Q_f)) \right), \quad \hat{K}_f = \rho_{3D} \left(\text{ReLU}(\text{RMSNorm}(K_f)) \right). \quad (12)$$

To keep the magnitude of the normalizer projection $K_f^\top S_f^z$ stable for large spatial token counts, both K_f and \hat{K}_f are additionally rescaled by $1/\sqrt{DN}$ before entering the recurrence. The unrotated key K_f is used for the normalizer state, while the rotated key \hat{K}_f is used for the KV memory update and readout; this “RoPE-on-numerator-only” choice preserves mass conservation in the linear-attention denominator, since rotated \hat{K}_f does not sum to a positive scalar after frame-wise accumulation.

G.3. Gate parameterization

The block predicts three gates: a frame-wise decay gate α_f , a token-wise write gate β_f , and an output gate G_f .

Decay gate α_f . We adopt a Mamba-style discretized state-space parameterization [11] for the decay gate, which empirically yields substantially more stable long-horizon recurrence than a plain sigmoid:

$$\bar{x}_f = \frac{1}{N} \sum_{n=1}^N (X_f)_{:,n} \in \mathbb{R}^D, \quad (13)$$

$$\Delta_f = \text{softplus}(W_\alpha \bar{x}_f + b_\alpha) \in \mathbb{R}_{>0}, \quad \alpha_f = \exp(-e^{A_{\log}} \cdot \Delta_f) \in (0, 1], \quad (14)$$

where $W_\alpha \in \mathbb{R}^{1 \times D}$ projects the spatially pooled frame feature \bar{x}_f to a scalar, $b_\alpha \in \mathbb{R}$ is a bias, and $A_{\log} \in \mathbb{R}$ is a learnable per-head log-rate parameter that ensures $A = e^{A_{\log}} > 0$. The decay α_f is therefore a per-frame per-head scalar shared across all N spatial positions and all D channels of the head. This parameterization is equivalent to the discretization $\alpha = e^{-A\Delta}$ of a continuous-time linear ODE with data-dependent step size Δ , and matches the selective-scan gating of Mamba-2.

Write gate β_f . The write gate is a token-wise sigmoid:

$$\beta_f = \text{sigmoid}(W_\beta X_f + b_\beta) \in (0, 1)^{1 \times N}, \quad (15)$$

where $W_\beta \in \mathbb{R}^{1 \times D}$ produces a single scalar per token (per head). For convenience we write

$$B_f = \text{Diag}(\beta_f) \in \mathbb{R}^{N \times N}$$

for its diagonal-matrix form, used in the matrix update equations below. The write gate controls how aggressively each token’s delta-rule correction is written into memory.

Output gate G_f . The output gate is a per-token, per-channel SiLU-modulated linear projection:

$$G_f = \text{SiLU}(W_g X_f + b_g) \in \mathbb{R}^{D \times N}, \quad (16)$$

where $W_g \in \mathbb{R}^{D \times D}$. This is analogous to the output gate of Gated Linear Attention [36] and the gated MLP of Mamba and serves as a fine-grained channel-wise selector on the attention output.

G.4. Frame-wise delta-rule update

At frame f , the previous recurrent states are first decayed:

$$\tilde{S}_f^{kv} = \alpha_f S_{f-1}^{kv}, \quad \tilde{S}_f^z = \alpha_f S_{f-1}^z. \quad (17)$$

The KV memory is then updated by a delta-rule correction in the spirit of fast-weight programmers [21, 35]:

$$S_f^{kv} = \tilde{S}_f^{kv} + (V_f - \tilde{S}_f^{kv} \hat{K}_f) B_f \hat{K}_f^\top. \quad (18)$$

Equivalently, this can be written in the compact delta-rule form

$$S_f^{kv} = \alpha_f S_{f-1}^{kv} (I - \hat{K}_f B_f \hat{K}_f^\top) + V_f B_f \hat{K}_f^\top. \quad (19)$$

The normalizer state is updated in the same correction-based manner, using the unrotated key K_f to preserve mass conservation:

$$S_f^z = \tilde{S}_f^z + K_f B_f (\mathbf{1} - K_f^\top \tilde{S}_f^z), \quad (20)$$

where $\mathbf{1} \in \mathbb{R}^N$ is an all-one vector. Equivalently,

$$S_f^z = \alpha_f (I - K_f B_f K_f^\top) S_{f-1}^z + K_f B_f \mathbf{1}. \quad (21)$$

The key difference from simple gated accumulation [36, 23] lies in the residual term

$$V_f - \tilde{S}_f^{kv} \hat{K}_f.$$

Instead of directly writing $V_f \hat{K}_f^\top$ into memory, GDN first *predicts* the current values from the decayed recurrent state and only writes back the remaining error, scaled by β_f . This correction-based update reduces interference between stored key/value associations [21], providing a more controlled finite-state memory for long streaming sequences. It is critical for minute-long streaming video generation where the same recurrent state must accumulate consistent identity and scene information across thousands of frames.

G.5. Normalized readout and output projection

After the recurrent states are updated, the output is obtained by a normalized linear-attention readout:

$$Y_f = \frac{S_f^{kv} \hat{Q}_f}{(S_f^z)^\top Q_f + \epsilon}, \quad (22)$$

where the numerator $S_f^{kv} \hat{Q}_f \in \mathbb{R}^{D \times N}$ uses the rotated query, the denominator $(S_f^z)^\top Q_f \in \mathbb{R}^{1 \times N}$ uses the unrotated query and is broadcast over the D channel dimension, and $\epsilon = 10^{-6}$ is a small constant for numerical stability. The final per-head output is produced by an element-wise multiplication with the output gate followed by a linear projection,

$$O_f = W_o(G_f \odot Y_f), \quad (23)$$

where $W_o \in \mathbb{R}^{D \times D}$ and \odot denotes the Hadamard product. Per-head outputs $\{O_f^{(h)}\}_{h=1}^H$ are then concatenated along the channel dimension and passed through a final shared linear projection.

G.6. Streaming cache

During streaming inference, each GDN block only caches the terminal states

$$(S^{kv}, S^z) \in \mathbb{R}^{D \times D} \times \mathbb{R}^D$$

per head from the previous chunk, and uses them to initialize the next chunk. The total cache size is therefore $\mathcal{O}(HD^2)$ per layer and is independent of the number of streamed chunks or the total streaming length. This allows the GDN blocks in SANA-Streaming to serve as a compact *global accumulated memory* that compresses the entire streaming history into a fixed-size matrix state, while the softmax blocks complement them by performing local window-and-sink refinement [30] over recent tokens.

H. Safeguards

For deployment, the model is paired with safeguards outside the generative model itself. We use a layered design in which policy checks are applied before generation, during generation when needed, and after generation before content is returned.

Input screening. User prompts and conditioning inputs is first checked by a policy classifier, such as Llama Guard [16] or an equivalent safety classifier. The classifier flags requests involving disallowed sexual content, minors, graphic violence, self-harm, instructions for wrongdoing, privacy violations, and other categories defined by the deployment policy. Prompts that clearly violate policy are rejected. Ambiguous prompts can be routed to a stricter policy, rewritten into a safe form, or sent for human review.

Generation-time controls. The generation service should preserve the original safety decision throughout sampling. For example, the system can attach a policy state to each request and avoid later prompt expansions that introduce disallowed entities or actions. Rate limits, authentication, and abuse monitoring should be applied to reduce automated misuse. For high-risk categories, the service can use conservative decoding settings or disable generation entirely rather than relying only on post-hoc filtering.

Output screening. Generated videos are checked before release. A practical implementation can sample frames from the beginning, middle, and end of each video, run an image or vision-language safety classifier on those frames, and optionally run OCR to detect unsafe or private text rendered in the video. If any sampled frame is flagged, the system blocks the video or route it to manual review. For applications with stricter requirements, all frames or short temporal clips can be screened instead of sparse frame samples.

Provenance and traceability. Generated content includes provenance metadata or a watermark when the deployment setting supports it. The service retains minimal audit logs needed for abuse investigation, including the safety decision, model version, and policy version, while avoiding unnecessary storage of sensitive user data.

Evaluation. Safeguards will be evaluated with a held-out red-team set covering direct policy violations, paraphrases, multilingual prompts, prompt-injection attempts, and benign prompts that are easy to over-block.

We report both block rates on unsafe prompts and false-positive rates on benign prompts. Because safety classifiers are imperfect, the safeguard layer should be treated as a risk reduction mechanism rather than a proof that unsafe outputs cannot occur.

I. Broader Impacts

SANA-Streaming enables real-time, high-quality video editing, which may benefit applications such as content creation, live broadcasting, and human–computer interaction. At the same time, such technology could be misused to generate misleading or manipulated video content, including real-time deepfakes or deceptive visual edits.

To mitigate these risks, our pipeline incorporates several safeguards, including VLM-based data verification to filter low-quality or misaligned samples, as well as instruction consistency and temporal stability checks during data construction. These measures aim to improve the faithfulness and reliability of generated content. However, we acknowledge that such safeguards are not sufficient to fully prevent misuse or unintended outcomes, especially in open or real-world deployment scenarios. Careful consideration of responsible deployment will be important to ensure that the technology is used in a socially beneficial manner.

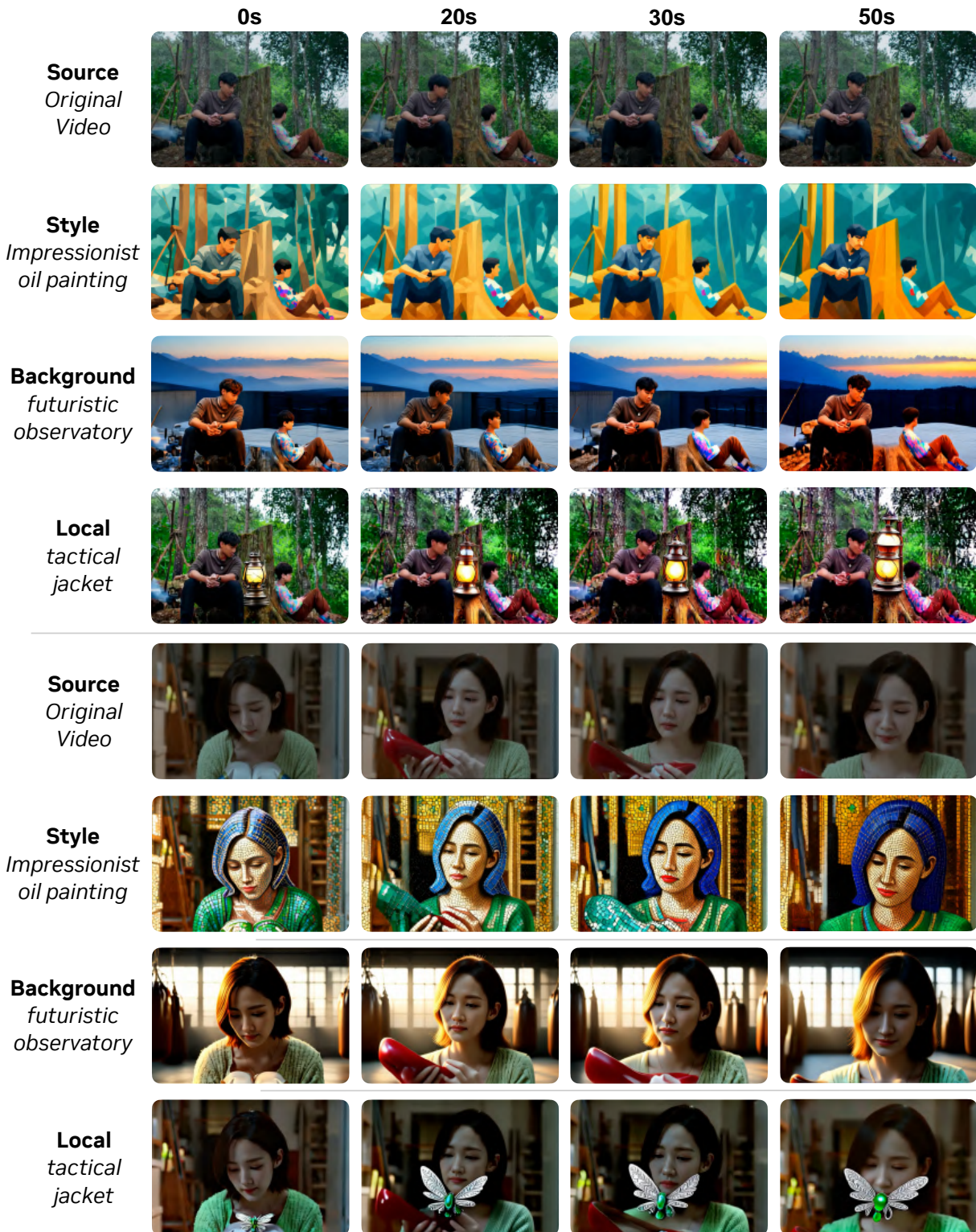


Figure 13 | **More visualizations.** SANA-Streaming follows editing instructions while preserving consistency with the original input videos.